**RESEARCH ARTICLE**

NMR IN BIOMEDICINE WILEY

# Cardiac cine magnetic resonance fingerprinting for combined ejection fraction, $T_1$ and $T_2$ quantification

Jesse I. Hamilton[1,2] | Yun Jiang[1,3] | Brendan Eck[2] | Mark Griswold[2,3] | Nicole Seiberlich[1,2,3]

[1]Department of Radiology, University of Michigan, Ann Arbor, Michigan, USA

[2]Department of Biomedical Engineering, Case Western Reserve University, Cleveland, Ohio, USA

[3]Department of Radiology, University Hospitals Cleveland Medical Center, Cleveland, Ohio, USA

**Correspondence**
Jesse I. Hamilton, Department of Radiology, University of Michigan, 1137 Catherine Street, Suite 1590B, Ann Arbor, MI 48109, USA.
Email: hamiljes@med.umich.edu

This study introduces a technique called cine magnetic resonance fingerprinting (cine-MRF) for simultaneous $T_1$, $T_2$ and ejection fraction (EF) quantification. Data acquired with a free-running MRF sequence are retrospectively sorted into different cardiac phases using an external electrocardiogram (ECG) signal. A low-rank reconstruction with a finite difference sparsity constraint along the cardiac motion dimension yields images resolved by cardiac phase. To improve SNR and precision in the parameter maps, these images are nonrigidly registered to the same phase and matched to a dictionary to generate $T_1$ and $T_2$ maps. Cine images for computing left ventricular volumes and EF are also derived from the same data. Cine-MRF was tested in simulations using a numerical relaxation phantom. Phantom and in vivo scans of 19 subjects were performed at 3 T during a 10.9 seconds breath-hold with an in-plane resolution of 1.6 x 1.6 mm$^2$ and 24 cardiac phases. Left ventricular EF values obtained with cine-MRF agreed with the conventional cine images (mean bias −1.0%). Average myocardial $T_1$ times in diastole/systole were 1398/1391 ms with cine-MRF, 1394/1378 ms with ECG-triggered cardiac MRF (cMRF) and 1234/1212 ms with MOLLI; and $T_2$ values were 30.7/30.3 ms with cine-MRF, 32.6/32.9 ms with ECG-triggered cMRF and 37.6/41.0 ms with $T_2$-prepared FLASH. Cine-MRF and ECG-triggered cMRF relaxation times were in good agreement. Cine-MRF $T_1$ values were significantly longer than MOLLI, and cine-MRF $T_2$ values were significantly shorter than $T_2$-prepared FLASH. In summary, cine-MRF can potentially streamline cardiac MRI exams by combining left ventricle functional assessment and $T_1$-$T_2$ mapping into one time-efficient acquisition.

**KEYWORDS**
cine, ejection fraction, low rank, magnetic resonance fingerprinting, myocardial tissue characterization, $T_1$ mapping, $T_2$ mapping

---

# 1 | INTRODUCTION

Cardiac MRI is the gold standard for functional assessment of the left ventricle (LV) and is often employed for myocardial tissue characterization.[1] However, cardiac MRI exams can be time-consuming due to the large number of different scans that must be performed. Cine scans are an essential part of most protocols and provide information about cardiac function, including ejection fraction (EF), myocardial mass and myocardial wall motion. Typically, a stack of 8-12 slices is acquired in short-axis view to cover the entire LV, with 1-2 slices imaged per breath-hold. Cardiac MRI protocols may also incorporate relaxation time mapping, which has gained interest recently. $T_1$ maps provide insight into inflammation,[2] fibrosis,[3] scar,[4,5] amyloid deposition[6] and fatty infiltrative diseases,[7] while $T_2$ changes may be related to edema,[8,9] iron deposition,[10] or early transplant rejection.[11] Although faster mapping scans have been demonstrated,[12] in routine clinical practice native $T_1$ and $T_2$ maps may only be acquired over a few slices due to time constraints, with each map requiring a separate breath-held scan. LV functional assessment and relaxation time mapping taken together require several minutes of repeated breath-holds. These scans are tiring for patients, and failed breath-holds may lead to image artifacts or repeated scans.

Magnetic resonance fingerprinting (MRF) methods have been proposed for rapid and simultaneous quantification of $T_1$ and $T_2$ in multiple organs,[13-15] including the heart.[16] Cardiac MRF (cMRF) uses a time-varying pulse sequence to encode $T_1$ and $T_2$ information in the MRI signal timecourses. Data are collected using a highly undersampled spiral k-space trajectory. A dictionary of signal timecourses is generated using a Bloch equation simulation that models the net magnetization evolution. Then quantitative $T_1$ and $T_2$ maps are reconstructed by identifying the dictionary entry that best matches the measured signal at each pixel. Because the scan is electrocardiogram (ECG)-triggered, the cardiac rhythm alters the sequence timings and hence the shape of the cMRF signal evolutions, so a new dictionary is simulated after each acquisition to obtain accurate $T_1$ and $T_2$ estimates. In addition to heart rate, cMRF can compensate for other sources of measurement error by modeling these effects in the dictionary. Slice profile imperfections, preparation pulse efficiency and $B_1^+$ inhomogeneities can be corrected in this way, potentially leading to more accurate and reproducible measurements.[17-19]

However, prospective ECG triggering is inefficient because data are only collected during part of the cardiac cycle. A single acquisition that combines relaxation time mapping with cine imaging to evaluate LV function would streamline the cardiac MRI exam workflow by reducing the total number of breath-holds. Additionally, the cine images, $T_1$ maps and $T_2$ maps would be inherently coregistered, which is not possible if these data are collected in separate acquisitions.

Recently, several novel techniques have been proposed for cardiac phase-resolved relaxation time mapping. Joint cine imaging and $T_1$ mapping techniques have been developed based on continuous Look-Locker acquisitions.[20-22] Methods that perform simultaneous $T_1$-$T_2$ mapping and cine imaging have also been demonstrated using continuous spoiled gradient echo readouts interrupted by inversions and $T_2$ preparation pulses. One such approach has been combined with golden angle radial k-space sampling and a low-rank patch-based (HD-PROST) reconstruction to achieve 3D coverage.[22,23] Another approach is CMR multitasking, which uses a nongated, free-breathing acquisition with a low-rank tensor reconstruction to achieve 2D phase-resolved $T_1$ and $T_2$ mapping.[24,25]

The goal of this study is to extend cMRF to a free-running and retrospectively gated acquisition called cine-MRF. The main motivation is to improve efficiency by simultaneously obtaining coregistered $T_1$ and $T_2$ maps and cine images from one acquisition that has the same breath-hold duration as a standard cine scan. A secondary goal is to achieve superior temporal resolution compared with prospectively ECG-triggered mapping sequences, including ECG-triggered cMRF, by using nonrigid image registration. Cine-MRF was evaluated in numerical simulations with a moving cardiac phantom, and it was compared with ECG-triggered cMRF and conventional sequences by scanning the ISMRM/NIST MRI system phantom and 19 healthy subjects at 3 T.

# 2 | EXPERIMENTAL

The following sections describe the different steps in the cine-MRF data processing workflow. Briefly, k-space data from a continuous MRF acquisition are retrospectively binned into different cardiac phases using an ECG signal. A low-rank reconstruction is performed that yields images in a low-dimensional subspace over multiple cardiac phases. These images are nonrigidly registered to the same target cardiac phase and matched to the dictionary to generate $T_1$ and $T_2$ maps. Contrast-weighted cine images are obtained from the same dataset for calculating ventricular volumes and EF.

## 2.1 | Pulse sequence and data acquisition

In cine-MRF, data are acquired using a free-running sequence with variable flip angles, inversions and $T_2$ preparations. The sequence uses a fast imaging with steady-state precession (FISP) readout because of its relative insensitivity to off-resonance.[26] The scan consists of 2060 repetition times (TRs) collected during a 10.9-second breath-hold. The flip angle pattern is comprised of 20 half-sinusoids, referred to as segments. Within

each segment, the flip angles range from 4° to a maximum value no greater than 15°. A nonselective hyperbolic secant inversion is applied every five segments beginning with the first segment, or approximately every 2.7 seconds, with an inversion time (TI) of 20.6 ms. Nonselective $T_2$ preparation pulses with BIR-4 tip-down and tip-up pulses and an MLEV refocusing train[27] are applied every third, fourth and fifth segment with variable echo times ($TE_{T2prep}$) between 30-80 ms. The cine-MRF acquisition parameters are provided in Additional File 1 (see the supporting information).

Data are acquired using a variable density spiral k-space trajectory with minimum-time gradient design and 0th moment compensation.[28] The spiral requires 24 interleaves to fully sample the central 25% of k-space and 48 interleaves to fully sample the periphery of k-space, and it has a readout duration of 3.3 ms. The trajectory rotates by the golden angle every TR to produce spatially and temporally incoherent aliasing artifacts.[29]

## 2.2 | Dictionary simulation

The dictionary is constructed using a Bloch equation simulation with 500 spins and includes corrections for slice profile effects and preparation pulse efficiency.[17] All scans use a Hanning windowed sinc-shaped radiofrequency pulse with a time-bandwidth product of 2 and a duration of 0.8 ms. A total of 13 925 signal evolutions are simulated for $T_1$ [10:10:2000 2050:50:3000] ms and $T_2$ [4:2:80 85:5:120 130:10:300] ms. Combinations where $T_1 < T_2$ are excluded. The cine-MRF dictionary is only computed once because the sequence is free-running: the subject's cardiac rhythm affects how data are binned but does not change the sequence timings. This is in contrast to prospectively ECG-triggered cMRF, which requires scan-specific dictionary generation because the cardiac rhythm influences the timings of each acquisition window. The cine-MRF dictionary occupies 200 MB of memory and takes 4 minutes to simulate on a workstation with 12 CPU cores running parallelized MATLAB Mex code.

## 2.3 | Low-rank reconstruction

The k-space readouts are retrospectively binned into different cardiac phases using the recorded ECG signal (Figure 1). Each RR interval is divided into 24 equally spaced phases, which is similar in number and temporal resolution to a conventional cine scan. The same number of readouts is not necessarily assigned to each phase due to variations in heart rate. On average, only 86 readouts (2060 TRs/24 phases) are grouped into each phase. Thus, the data are highly undersampled considering that most MRF techniques employ sequence lengths of hundreds to thousands of TRs (note that the prior work with ECG-triggered cMRF used 768 TRs).[16]
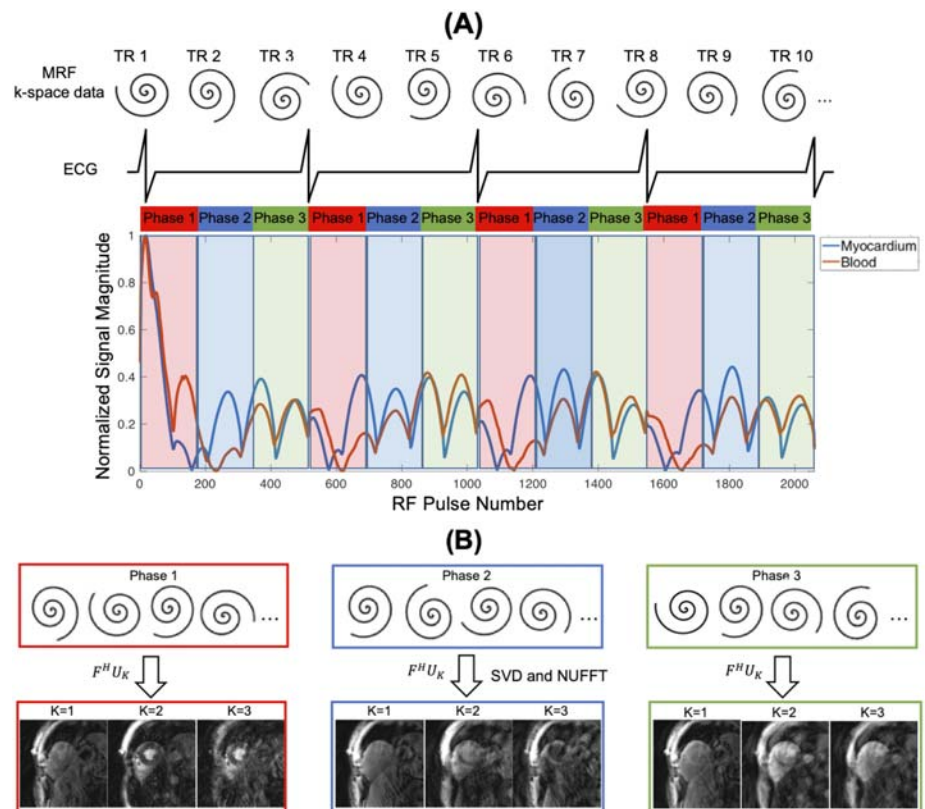


FIGURE 1 Cardiac phase binning. (A) The MRF spiral k-space readouts are retrospectively binned into different cardiac phases using an external ECG signal. Each RR interval is divided into 24 equally spaced bins, although only three are shown for clarity. Cine-MRF signal evolutions representative of myocardium ($T_1$ = 1400 ms/$T_2$ = 50 ms) and blood ($T_1$ = 2000 ms/$T_2$ = 300 ms) are also plotted. (B) A low-dimensional subspace is computed from the SVD of the MRF dictionary. The binned k-space data are projected onto this subspace and gridded to the image domain using the NUFFT. This work compresses the dictionary to rank 5, although only the first three (K = 1 through K = 3) subspace images are shown for clarity

Next, a low-rank reconstruction is performed to jointly reconstruct images at every cardiac phase that reside in a low-dimensional subspace derived from the dictionary (Figure 2). The reconstruction is reminiscent of XD-GRASP[30] and of low-rank methods that have been described for parameter mapping.[31-34] Let $D$ denote the cine-MRF dictionary with size $T$ (number of TRs) x $P$ (number of $T_1$ and $T_2$ combinations). In this study, $T$ = 2060 and $P$ = 13 925. A low-rank approximation to the dictionary is found by computing the singular value decomposition (SVD) of the dictionary along the time dimension and only retaining the first K columns of the left singular matrix $U$ corresponding to the K largest singular values, denoted by $U_K$.[35] The rank K is selected as the number of singular values that are larger than 3% of the first singular value, which yields K = 5 for this pulse sequence. A compressed dictionary $D_K$ with size $K$ x $P$ is obtained by

$$D_K = U_K D \tag{1}$$

The time series of undersampled cine-MRF images can also be projected to a set of images $\tilde{x}$ in the low-dimensional subspace, hereafter called "subspace images".

$$\tilde{x} = U_K x \tag{2}$$

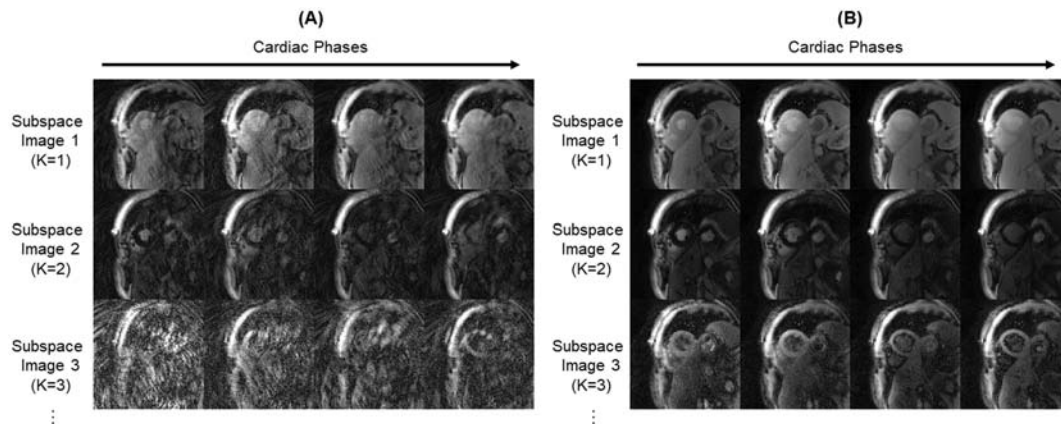The low-rank reconstruction is formulated as an $l_1$-minimization problem,

$$\min_{\tilde{x}} \left( \sum_{i=1}^M \left\| P_i \left( y - U_K^H F S \tilde{x}_i \right) \right\|_2^2 \right) + \lambda_1 \| \Psi_1 \tilde{x} \|_1 + \lambda_2 \| \Psi_2 \tilde{x} \|_1. \tag{3}$$

In Equation 3, $M$ = 24 is the number of phases; $\tilde{x}_i$ denotes the subspace images for phase $i$ and has size $N_y \times N_x \times K$, where $N_y$ and $N_x$ are the size of the x- and y-dimensions of the image; $\tilde{x}$ denotes the subspace images for all phases and has size $N_y \times N_x \times K \times M$; $S$ denotes the coil sensitivity maps; $F$ is the nonuniform fast Fourier Transform (NUFFT)[36]; $y$ is the acquired k-space data; and $P_i$ is a sampling mask that extracts only those k-space readouts that fall within the temporal window of phase $i$.

Two sparsifying transforms are applied to the subspace images: Daubechies wavelets ($\Psi_1$) along the spatial dimensions and finite differences ($\Psi_2$) along the cardiac motion dimension. The regularization weights were chosen empirically by reconstructing several in vivo datasets with different $\lambda_1$ and $\lambda_2$ values and selecting parameters that visually yielded the best suppression of noise, reduction of spiral aliasing artifacts, and preservation of temporal dynamics (relative to the subspace images before the low-rank reconstruction). Figure 3 shows the effect of varying the temporal finite difference penalty. All data shown in this work are reconstructed with $\lambda_1$= 0.001 and $\lambda_2$= 0.01 scaled relative to the maximum intensity in the subspace images. To estimate coil sensitivity maps, the subspace images that correspond to the first singular value are averaged over all cardiac phases before using the Walsh method.[37] Equation 3 is solved using nonlinear conjugate gradient descent with backtracking line search and a fixed 100 iterations,[38] and the resulting images are hereafter called "reconstructed subspace images".

## 2.4 | Nonrigid registration and pattern matching

The reconstructed subspace images for each cardiac phase are nonrigidly registered to the same phase before performing pattern matching to improve the SNR and precision of the parameter maps. Deformation fields are computed using the reconstructed subspace images that correspond to the second singular value because they were empirically found to have high contrast between myocardium and blood. Deformation



**FIGURE 2** Low-rank reconstruction. Subspace images are shown for several different cardiac phases (A) before and (B) after performing the low-rank reconstruction. For clarity, only three subspace images for four cardiac phases are shown. The low-rank reconstruction reduces the appearance of spiral undersampling artifacts

**FIGURE 3** Choice of temporal finite difference penalty in the low-rank reconstruction. (A) Reconstructed subspace images are shown corresponding to the second singular value (K = 2) in diastole and systole. The temporal finite difference penalty ($\lambda_2$) is varied from 0 to 0.05, scaled relative to the maximum image intensity, and the spatial Wavelet penalty is fixed at $\lambda_1$=0.001. When the temporal regularization penalty is too low ($\lambda_2$= 0 and $\lambda_2$= 0.001), the images are corrupted by residual artifacts and noise enhancement. However, when the regularization penalty is too large ($\lambda_2$= 0.05), there is temporal blurring along the cardiac motion dimension. A value of $\lambda_2$= 0.01 is used for all datasets in this work and provides a tradeoff between artifact reduction and temporal fidelity. (B) A line profile was drawn through the heart. (C) Plots of the line profile over all cardiac phases are shown. For small values of $\lambda_2$, the profiles appear noisy but have good temporal fidelity. Temporal blurring is observed when $\lambda_2$ is too large ($\lambda_2$= 0.05). A value of $\lambda_2$= 0.01 reduces noise and artifacts while preserving the temporal dynamics
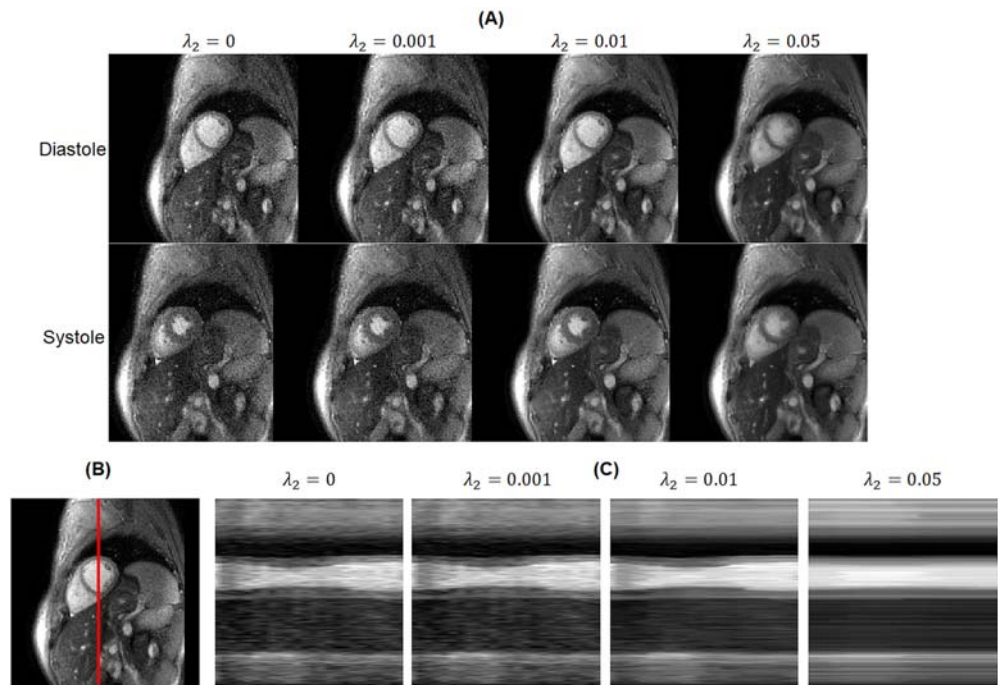


fields are calculated and saved between every possible pair of cardiac phases (eg, phase 1→2, 1→3, ..., 24→22, 24→23). In total, there are 24 x 23 = 552 pairs of phases. This step is implemented in R using the open-source RNiftyReg software with a mutual information cost function.[39,40] Other parameters include a 3 x 3 final grid spacing, three multi-resolution levels, a maximum of 500 iterations per level, and 28 histogram intensity bins.

Next, a target phase is selected, and all the reconstructed subspace images are registered to the target phase using the deformation fields (Figure 4). For example, if phase 1 is chosen as the target phase, the reconstructed subspace images from phases 2 through 24 are spatially aligned to phase 1. After registration, the images are complex-averaged over the cardiac phase dimension to improve SNR. The complex-valued signal at each pixel in the registered subspace images is compared with the compressed dictionary $D_K$ using dot product matching to generate quantitative maps of $T_1$ and $T_2$ for phase 1. Image registration and pattern matching are repeated, each time choosing a different target phase, to construct $T_1$ and $T_2$ maps spatially aligned to every phase in the cardiac cycle. The use of image registration allows data from the entire scan to be used for pattern matching, thereby improving the SNR and precision of the parameter maps. The reconstructed subspace images that correspond to the second singular value are also used as cine images for evaluating LV function.

## 2.5 | Numerical simulations

Cine-MRF was investigated in two simulation experiments using the MRXCAT numerical cardiac phantom.[41] The phantom has 24 cardiac phases, modified to reflect relaxation times relevant for 3 T MRI. Respiratory motion was not simulated since data are collected during a breath-hold. Motion states were assigned using an ECG recorded from an in vivo volunteer scan where the heart rate varied from 71-82 bpm.
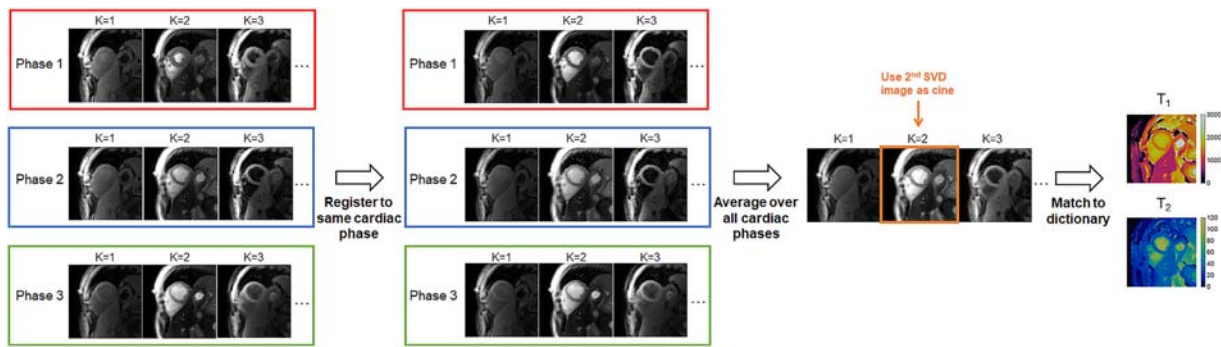
**FIGURE 4** Image registration and pattern matching. The leftmost panel shows reconstructed subspace images corresponding to the first three singular values (K = 1 through K = 3) for three cardiac phases. Phase 1 is in systole, while phases 2 and 3 are in diastole. Next, nonrigid deformation fields are used to register the images to the same phase. In this example, phase 3 is selected as the target phase. The registered images are then averaged over the cardiac phase dimension and matched to the dictionary to generate $T_1$ and $T_2$ maps. Additionally, the image corresponding to the second singular value (highlighted in orange) is used as a cine frame. Image registration and pattern matching are repeated, each time registering the reconstructed subspace images to a different cardiac phase to generate maps and cine images throughout the cardiac cycle

In the first experiment, the ground truth myocardial values were fixed at $T_1$ = 1410 ms and $T_2$ = 50 ms. Maps were reconstructed using three approaches. In the first approach, the low-rank reconstruction was performed without binning data into different cardiac phases. This is equivalent to solving Equation 3 with one cardiac phase and no temporal regularization ($\lambda_2$= 0). In the second approach, data were binned into 24 phases and reconstructed using the low-rank method. However, the reconstructed subspace images for each cardiac phase (ie, the images depicted in Figure 2B) were matched to the dictionary without image registration. In the third approach, the reconstructed subspace images were registered (as shown in Figure 4) so that all the collected data could be used for pattern matching. Accuracy was evaluated by measuring the relative percent deviation from the ground truth $T_1$ and $T_2$ values in the myocardium. Precision was quantified using the coefficient of variation (CV), defined as the standard deviation in $T_1$ (or $T_2$) divided by the reference value in the myocardium. Image sharpness was evaluated by measuring the myocardial wall thickness. Line profiles were drawn across the septum in the $T_1$ and $T_2$ maps for every phase. Wall thickness was defined as the number of pixels along the profile having $T_1$ (or $T_2$) within 10% of the ground truth $T_1$ (1410 ms) or $T_2$ (50 ms) for myocardium.

The second experiment explored the performance of cine-MRF when the underlying tissue property values are changing. The ground truth myocardial $T_1$ and $T_2$ values were gradually swept from 1340 and 50 ms in diastole to 1400 and 44 ms in systole, respectively, and accuracy and precision were quantified as described above.

## 2.6 | Phantom experiments

The $T_2$ layer of the ISMRM/NIST MRI system phantom[42] was scanned at 3 T (Siemens MAGNETOM Skyra, Erlangen, Germany) using an 18-channel cardiac array coil and 12 channels from the built-in spine array. A cine-MRF scan was acquired with 192 x 192 matrix, 300 mm$^2$ FoV, 8 mm slice thickness, and 1.6 x 1.6 mm$^2$ resolution. Similar to the simulation experiments, 24 motion states were assigned using an ECG recorded during an in vivo scan, and maps were reconstructed using the proposed workflow. Since the phantom dataset has no motion, this experiment was intended to study the accuracy and precision in quantifying $T_1$ and $T_2$. The maps were analyzed by manually drawing regions of interest (ROIs) in each phantom sphere and measuring the mean and standard deviation in $T_1$ and $T_2$. Measurements were compared with reference values provided by NIST using Pearson's correlation and a Bland–Altman analysis.[43] Consistency throughout the cardiac cycle was quantified by computing the CV of the mean $T_1$ and $T_2$ values over all phases.

## 2.7 | In vivo volunteer imaging

Nineteen subjects with no self-reported history of cardiovascular disease were enrolled in this IRB-approved, HIPAA-compliant study after obtaining written informed consent. Cardiac scans were performed in short-axis orientation at a medial slice position with breath-holds in end-expiration. Volume shimming centered on the LV was performed. All scans were acquired with 192 x 192 matrix, 300 mm$^2$ FoV, 1.6 x 1.6 mm$^2$ resolution, and 8 mm slice thickness. In addition to cine-MRF, ECG-triggered cMRF scans were collected during a 16-heartbeat breath-hold with a 254 ms scan window.[16] Two separate acquisitions were performed with both diastolic and systolic scan windows. Due to the duration of the

longest $T_2$ preparation pulse, the minimum allowed trigger delay for the scan with the systolic scan window was 106 ms. A new dictionary was simulated for each ECG-triggered cMRF scan using the recorded ECG timings and including the same $T_1$ and $T_2$ ranges as the cine-MRF dictionary. Maps were reconstructed using a low-rank reconstruction described in previous cMRF work,[32] which is equivalent to Equation 3 with one cardiac phase and no temporal regularization ($\lambda_2 = 0$). Conventional $T_1$ and $T_2$ maps were acquired using Siemens MyoMaps.[44] The $T_1$ maps were collected using modified Look-Locker inversion recovery (MOLLI) with a 5(3)3 scheme (ie, five imaging heartbeats, three recovery heartbeats and three imaging heartbeats),[45] and $T_2$ maps were collected using $T_2$-prepared FLASH with a 1(3)1(3)1 scheme and echo times of 0, 25 and 55 ms. All MyoMaps scans were repeated with diastolic and systolic scan windows. The MyoMaps scans used GRAPPA with an acceleration factor 2 and 24 autocalibration lines, 6/8 partial Fourier, 35° flip angle, and a scan window of 209 ms. The maps were calculated inline at the scanner using curve fitting. A conventional cine scan with a balanced steady-state free precession (bSSFP) readout was acquired at a medial slice position with 24 phases, flip angle 35-70° (depending on the SAR limits), TR/TE 2.8/1.4 ms, GRAPPA acceleration factor 2 with 24 autocalibration lines, and BW 965 Hz/pixel. Conventional cine scans were not acquired in two subjects due to time constraints. To evaluate the performance of cine-MRF for functional assessment over the entire LV, both standard bSSFP cine and cine-MRF scans were acquired in six subjects over multiple slices (one breath-hold per slice). The number of slices in each short-axis stack ranged from 8 to 12 depending on the cardiac anatomy.

## 2.8 | In vivo data analysis

Maps were analyzed by manually drawing ROIs in six medial segments according to the standardized AHA model in diastolic and systolic phases, and the mean and standard deviation in $T_1$ and $T_2$ were measured for each segment.[46] For cine-MRF data, end-diastolic and end-systolic frames were identified as those with the largest and smallest blood pool volumes, respectively. The mean $T_1$ (and $T_2$) values in the septum were compared using a one-way ANOVA test with Tukey's posthoc correction with six groups, corresponding to the three techniques (cine-MRF, ECG-triggered cMRF and MyoMaps) and two cardiac phases (diastole and systole). The septal $T_1$ and $T_2$ values between cine-MRF versus ECG-triggered cMRF and cine-MRF versus conventional mapping methods were also visualized using Bland–Altman plots. The intrasubject CV was computed for each subject by dividing the standard deviation in $T_1$ (or $T_2$) by the mean value in a septal ROI to assess intrasubject variability. Then a one-way ANOVA test was performed using the same six groups as described previously. A $P$-value of below .05 was considered statistically significant. The inter-subject CV was calculated by taking the standard deviation of the mean $T_1$ (or $T_2$) values measured for each subject and dividing by the group-averaged $T_1$ (or $T_2$). To assess intrareader repeatability, all $T_1$ and $T_2$ maps were contoured during a second session by the same reader, and the intraclass correlation coefficient (ICC) for each myocardial segment's mean $T_1$ and $T_2$ values was computed.

To assess LV function, the endocardial borders were manually contoured on one diastolic and one systolic frame of the cine datasets. Single-slice EF was quantified using
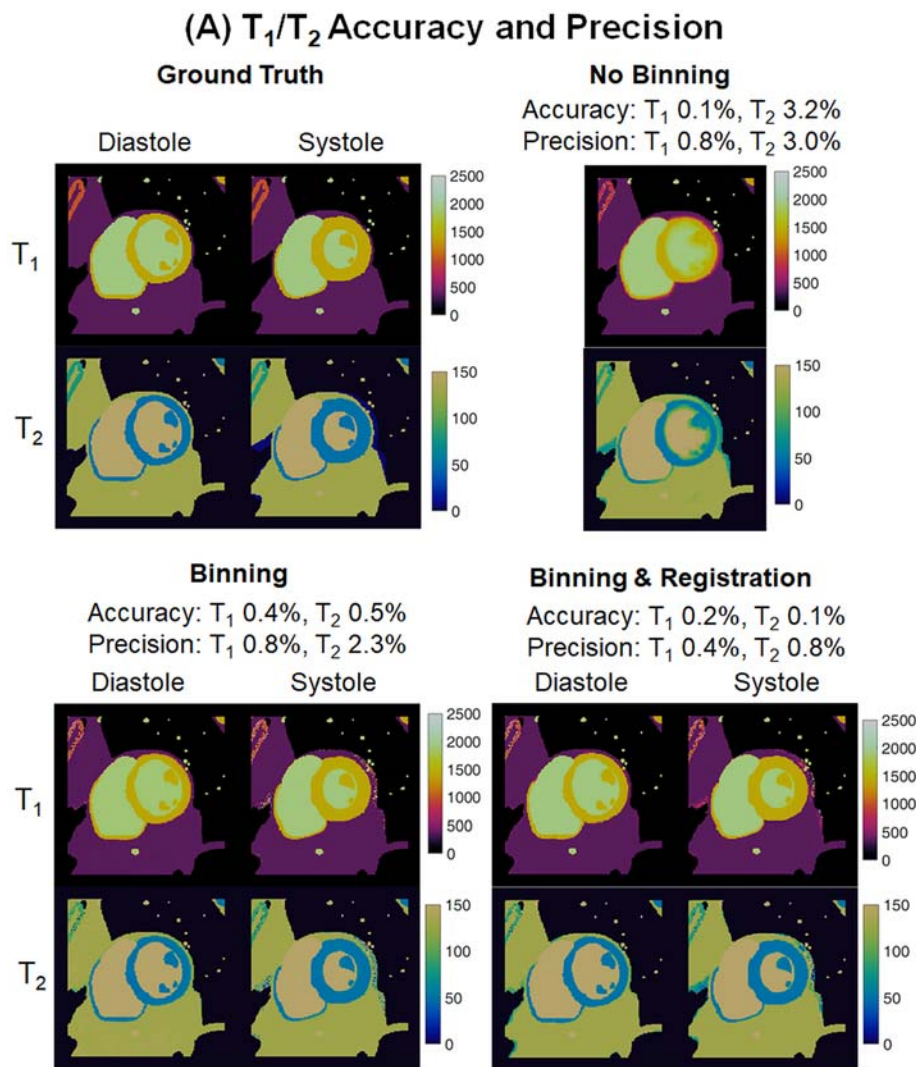
$$EF = \frac{EDV - ESV}{EDV} \times 100\%$$

(4)

where ESV and EDV are end-systolic volume and end-diastolic volume, respectively, excluding the papillary muscles. In the six datasets having whole LV coverage, EDV and ESV were computed for each slice and combined using Simpson's rule before calculating EF. Single-slice EF (17 out of 19 subjects) and whole-LV EDV, ESV and EF measurements (6 out of 19 subjects) from cine-MRF and the standard cine scans were compared using a Bland–Altman analysis. To quantify the blood-myocardium contrast, the average signal within ROIs in the LV blood pool and septal myocardium was measured in each subject and used to calculate a blood-to-myocardium signal intensity ratio for the standard bSSFP cine images and MRF-derived cine images.
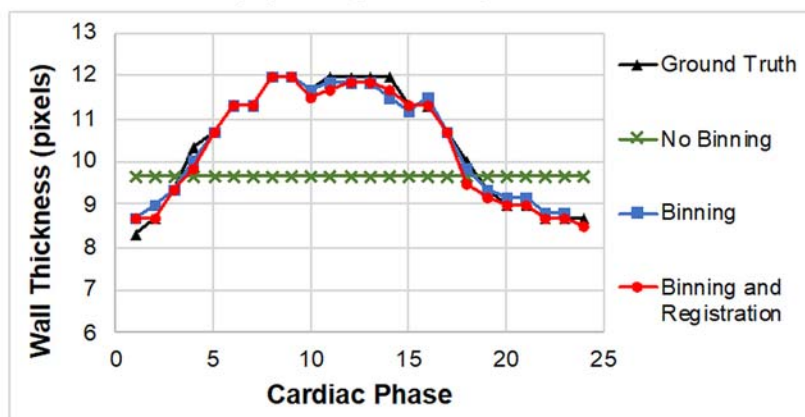
## 3 | RESULTS

### 3.1 | Numerical simulations

Results from the numerical simulations are shown in Figure 5. In these experiments, the ground truth $T_1$ and $T_2$ values were held fixed throughout the cardiac cycle. Maps reconstructed without cardiac phase binning (ie, assuming a single cardiac phase although the heart was moving) had a relative error of 0.1% for $T_1$ and 3.2% for $T_2$, and a CV of 0.8% for $T_1$ and 3.0% for $T_2$. However, the maps suffered from motion artifacts and blurring, which is observed quantitatively in Figure 5B, where the myocardial wall thickness in the reconstructed maps (10 pixels) is larger than the thickness in the ground truth maps at diastole (8 pixels). After binning the data into 24 phases and using the low-rank reconstruction, the maps had improved accuracy for $T_2$ (relative error of 0.4% for $T_1$ and 0.5% for $T_2$) and slightly improved precision for $T_2$ (CV of 0.8% for $T_1$ and 2.3% for $T_2$). The measured wall thickness was consistent with the reference thickness. The combination of cardiac phase binning, low-rank

## (A) $T_1/T_2$ Accuracy and Precision

**Ground Truth**

Diastole | Systole

$T_1$

$T_2$

**No Binning**
Accuracy: $T_1$ 0.1%, $T_2$ 3.2%
Precision: $T_1$ 0.8%, $T_2$ 3.0%

**Binning**
Accuracy: $T_1$ 0.4%, $T_2$ 0.5%
Precision: $T_1$ 0.8%, $T_2$ 2.3%

Diastole | Systole

$T_1$

$T_2$

**Binning & Registration**
Accuracy: $T_1$ 0.2%, $T_2$ 0.1%
Precision: $T_1$ 0.4%, $T_2$ 0.8%

Diastole | Systole

$T_1$

$T_2$



**FIGURE 5** Simulation results under conditions of constant ground truth $T_1$ and $T_2$. (A) $T_1$ and $T_2$ maps are shown for representative diastolic and systolic frames. Results are shown for (top left) the ground truth, (top right) low-rank reconstruction with no motion binning, (bottom left) low-rank reconstruction using 24 cardiac phases, and (bottom right) low-rank reconstruction with 24 cardiac phases followed by nonrigid registration. Measures of accuracy (relative percent error in myocardial $T_1$ and $T_2$) and precision (coefficient of variation) are reported. (B) Image sharpness (ie, apparent myocardial wall thickness) is plotted for each technique

## (B) Image Sharpness



reconstruction and image registration yielded the best results in terms of accuracy (relative error of 0.2% for $T_1$ and 0.1% for $T_2$) and precision (CV of 0.4% for $T_1$ and 0.8% for $T_2$), and the measured wall thickness agreed with the reference thickness.

In the second simulation, the ground truth myocardial $T_1$ and $T_2$ values changed throughout the cardiac cycle. Figure 6 shows the mean and standard deviation in the measured relaxation times at different cardiac phases. The low-rank reconstruction without cardiac phase binning (ie, assuming a single phase) yielded $T_1$ and $T_2$ values that are an average of the true diastolic and systolic relaxation times (1365.8 ms for $T_1$ and 48.3 ms for $T_2$). After binning the data into 24 phases and using the low-rank reconstruction, changes in $T_1$ and $T_2$ throughout the cardiac cycle

**FIGURE 6** Simulation results under conditions with variable ground truth $T_1$ and $T_2$ throughout the cardiac cycle. (A) The ground truth $T_1$ increased from 1340 ms in diastole to 1400 ms in systole, (B) while the ground truth $T_2$ decreased from 50 ms in diastole to 44 ms in systole. The ground truth values are plotted in black, the low-rank reconstruction with 24 cardiac phases is plotted in blue, and the low-rank reconstruction with 24 phases and nonrigid registration is plotted in red



(A) $T_1$

(B) $T_2$
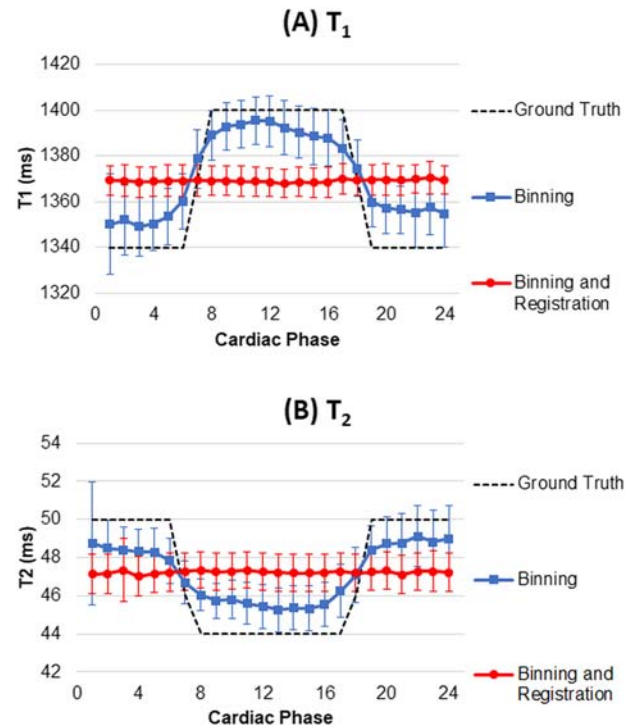
were observed, although the longest $T_1$ and $T_2$ values were underestimated and the shortest $T_1$ and $T_2$ values were overestimated. The low-rank reconstruction followed by nonrigid registration was not able to track the dynamics in $T_1$ and $T_2$ and instead yielded an average of the diastolic and systolic relaxation times. However, the maps had improved precision compared with the low-rank reconstruction without registration (see discussion above and precision measurements in Figure 5).

## 3.2 | Phantom experiments

Phantom validation was performed using the ISMRM/NIST MRI system phantom with motion states assigned to the data using an ECG recorded from a separate in vivo scan. Figure 7A shows the mean $T_1$ and $T_2$ measured within each phantom sphere over different phases. The cine-MRF relaxation times showed high consistency throughout the cardiac cycle ($T_1$ CV 0.30% ±0.26% and $T_2$ CV 0.76%±0.81%). Figure 7B shows a linear regression comparing the reference $T_1$ and $T_2$ values provided by NIST with cine-MRF measurements that were averaged over all phases. A Bland–Altman plot of the same data is provided in Figure 7C. The mean bias for $T_1$ is 4.6 ms with 95% limits of agreement (−29.8, 39.0) ms, and the mean bias for $T_2$ is −1.5 ms with 95% limits of agreement (−11.1, 8.2) ms.

## 3.3 | In vivo volunteer imaging

Examples of $T_1$ and $T_2$ maps in diastole and systole for cine-MRF, ECG-triggered cMRF and MyoMaps (MOLLI and $T_2$-prepared FLASH) are displayed in Figure 8A. Relaxation times measured in a septal ROI are provided on the insets. Note that it was not possible to capture the earliest part of systole using ECG-triggered cMRF and MyoMaps due to the long scan window (254 ms for ECG-triggered cMRF and 209 ms for MyoMaps), which may account for the different position of the myocardial wall. Figure 8B shows diastolic and systolic frames from the cine images derived from cine-MRF and the conventional cine. Additional examples of cine-MRF $T_1$ and $T_2$ maps and cine images in movie format are provided in Supporting Videos 1-4 (see the supporting information).

Figure 9 summarizes the $T_1$ and $T_2$ values for each myocardial segment in diastole and systole averaged over all subjects. Over the entire myocardium in the medial slice, the average diastolic/systolic $T_1$ values were: cine-MRF 1397.7/1391.4 ms, ECG-triggered cMRF 1394.4/1378.0 ms and MOLLI 1234.2/1212.1 ms. The average diastolic/systolic $T_2$ times were: cine-MRF 30.7/30.3 ms, ECG-triggered cMRF 32.6/32.9 ms and $T_2$-prepared FLASH 37.6/41.0 ms. No significant differences were observed between cine-MRF and ECG-triggered cMRF $T_1$ and $T_2$ values, either in diastole or systole. The mean $T_1$ times measured with both cine-MRF and ECG-triggered cMRF were significantly higher than MOLLI in both diastolic and systolic phases ($P < .01$). The mean $T_2$ values measured with cine-MRF and ECG-triggered cMRF were
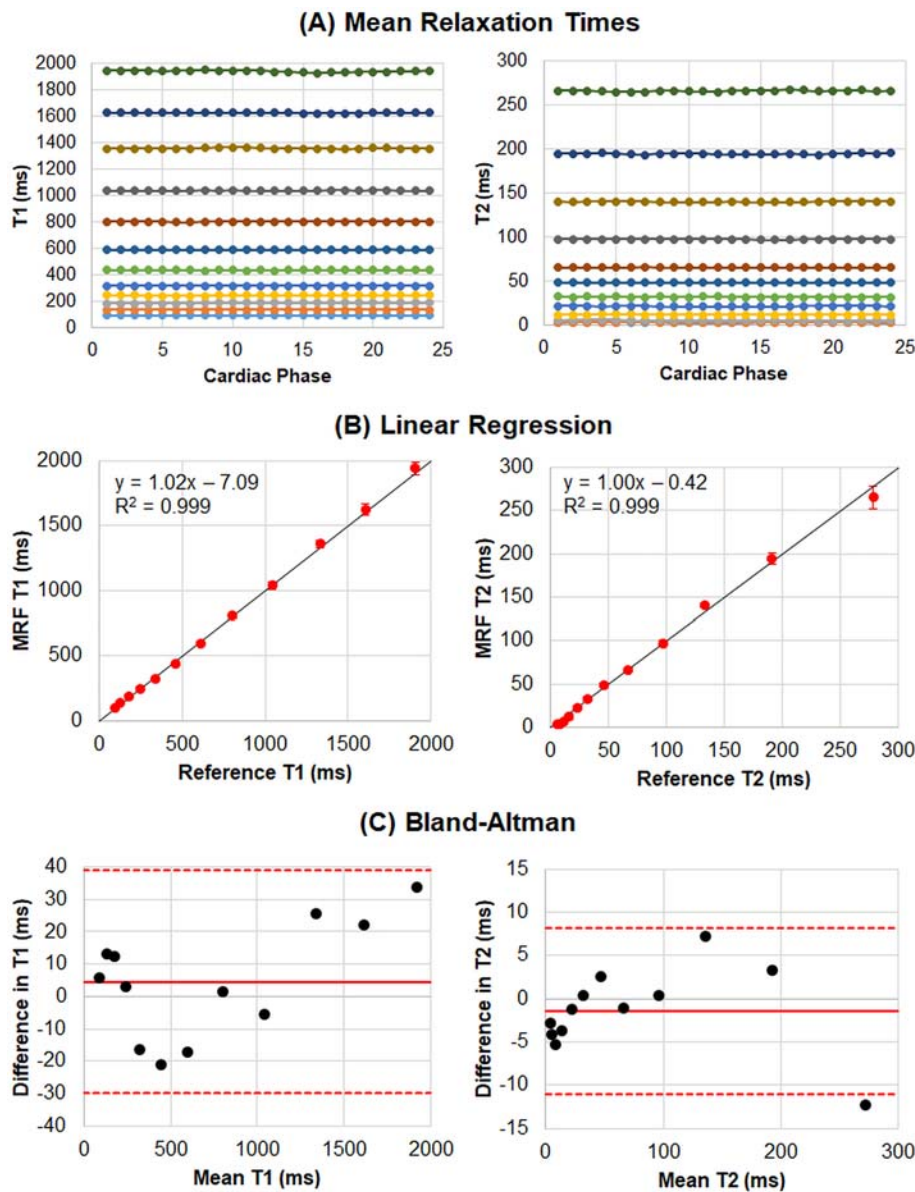
**FIGURE 7** Cine-MRF results using the ISMRM/NIST MRI system phantom at 3 T. (A) Phantom $T_1$ and $T_2$ times are compared across cardiac phases. (B) Linear regression comparing reference values with relaxation times measured using cine-MRF averaged over all phases. The identity line is plotted in black, and the best-fit line and Pearson's correlation are reported. (C) Bland–Altman plots comparing reference values with relaxation times measured using cine-MRF averaged over all phases. For $T_1$, the bias is 4.6 ms and 95% limits of agreement are (−29.8, 39.0) ms. For $T_2$, the bias is −1.5 ms and 95% limits of agreement are (−11.1, 8.2) ms

significantly lower than $T_2$-prepared FLASH in both diastole ($P < .05$) and systole ($P < .01$). No significant differences were observed between diastolic versus systolic relaxation times using cine-MRF or ECG-triggered cMRF. Mean $T_2$ times were significantly higher in systole compared with diastole using $T_2$-prepared FLASH ($P < .05$). Bland–Altman plots comparing the mean $T_1$ and $T_2$ values acquired with cine-MRF, ECG-triggered cMRF and conventional mapping sequences are shown in Figures 10 and 11.

For $T_1$, no significant differences in intrasubject CV were observed between methods or in diastolic versus systolic phases (Figure 12A). For $T_2$, no significant differences in intrasubject CV were seen between methods in diastole. For the systolic maps, the intrasubject CV for both cine-MRF and $T_2$-prepared FLASH were significantly higher than ECG-triggered cMRF ($P < .05$). As shown in Figure 12B, all techniques had a similar intersubject CV for $T_1$. For $T_2$, cine-MRF had the highest intersubject variability (7.7% in diastole, 9.2% in systole), followed by ECG-triggered cMRF (6.4% in diastole, 8.7% in systole), and $T_2$-prepared FLASH had the lowest intersubject variability (5.3% in diastole, 6.5% in systole).

Graphs from the intrareader repeatability study are shown in Additional File 2 (see the supporting information). For $T_1$, the ICC for cine-MRF and ECG-triggered cMRF was above 0.9 for all segments, indicating excellent intrareader repeatability. For MOLLI, the ICC was above 0.9 for segments 7-9 and segment 12; however, the ICC was lower at 0.87 for segment 10 and 0.67 for segment 11. For $T_2$, all methods had ICC values above 0.9 for every segment, with the one exception being segment 11 for cine-MRF (ICC 0.87).

Figure 13 shows an example of contrast-weighted cine images from cine-MRF and the corresponding standard cine images in a healthy subject at multiple slice positions covering the LV. Supporting Video 5 shows these datasets in movie format. When averaged over all subjects, the standard cine images had slightly higher CNR, with a blood-to-myocardium signal intensity ratio of 3.91 +/− 0.44 compared with 3.55 +/− 0.20 for the MRF-derived cine images. Figure 14 shows Bland–Altman plots of the LV functional measurements. For single-slice EF, good agreement
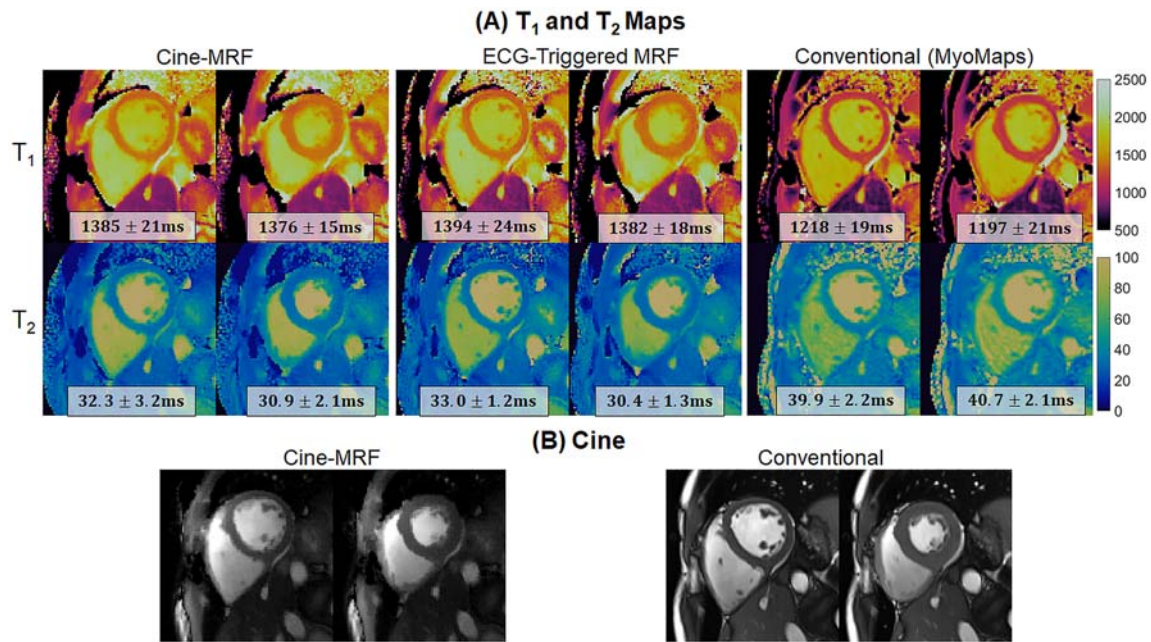
**FIGURE 8** Comparison of cine-MRF, ECG-triggered cardiac MRF and conventional scans in a subject at 3 T. (A) Examples of cine-MRF $T_1$ and $T_2$ maps in diastole and systole are shown. For comparison, maps were also collected with ECG-triggered cMRF, MOLLI and $T_2$-prepared FLASH. The ECG-triggered scans were repeated twice with the scan window placed once in diastole and once in systole. (B) Examples of cine images derived from the cine-MRF scan (left) compared with a conventional cine (right). Although cine-MRF uses a FISP-based readout with variable sequence parameters and the conventional cine uses a bSSFP readout, the image contrast in both datasets is quite similar with blood appearing bright and myocardium appearing dark

**FIGURE 9** Relaxation times measured in each medial myocardial segment in healthy subjects at 3 T. The mean (A) $T_1$ and (B) $T_2$ values measured in different myocardial segments at a medial slice are presented for cine-MRF, ECG-triggered cMRF and MyoMaps (MOLLI for $T_1$ mapping and $T_2$-prepared FLASH for $T_2$ mapping). Results are shown for diastolic and systolic phases. The error bars indicate the standard deviation across subjects
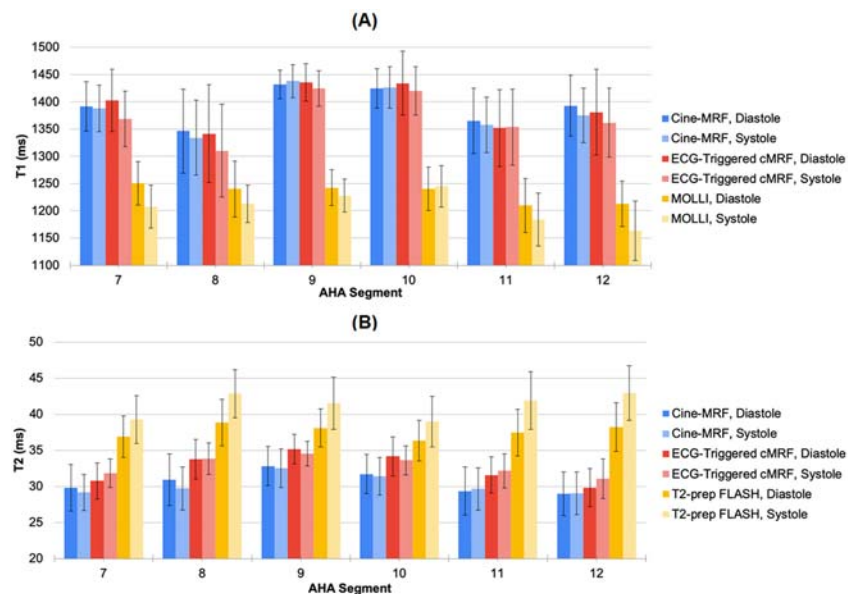


was observed between the standard cine scan and cine-MRF with a mean bias of −0.3% and 95% limits of agreement (−3.4%, 2.7%). Over the entire LV, the mean bias in EF was −1.0% with 95% limits of agreement (−3.4%, 1.3%). For EDV, the mean bias was 2.2 mL with 95% limits of agreement (−6.9 mL, 11.3 mL). For ESV, the mean bias was 1.9 mL with 95% limits of agreement (−2.3 mL, 6.2 mL).

## 4 | DISCUSSION

The motivation behind this work was to streamline the typical cardiac MRI exam by combining LV functional assessment and $T_1$-$T_2$ mapping into a single acquisition. A novel technique called cine-MRF was introduced for simultaneously generating $T_1$ and $T_2$ maps and cine images for
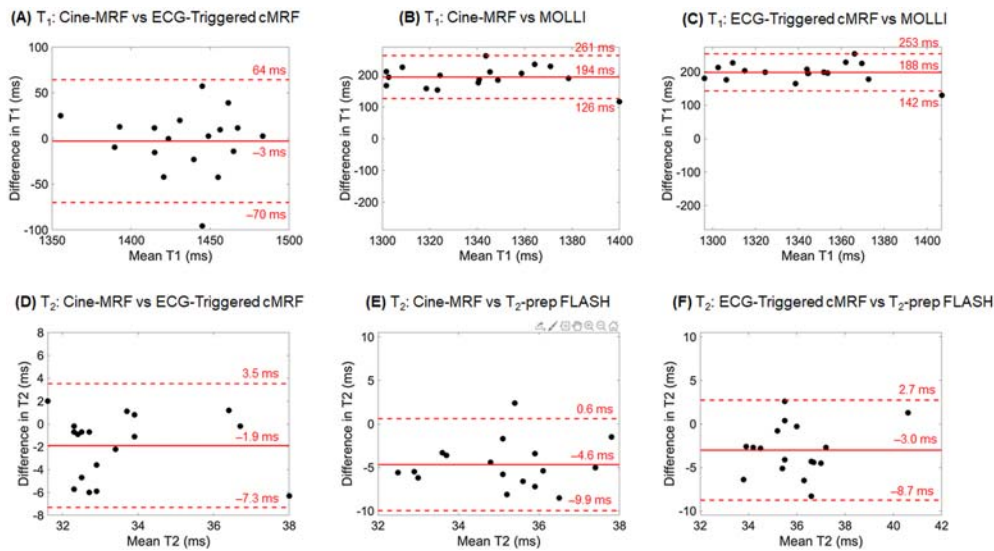
**FIGURE 10** Bland–Altman plots comparing mean diastolic myocardial $T_1/T_2$ values. These plots compare $T_1$ values between (A) cine-MRF and ECG-triggered cMRF, (B) cine-MRF and MOLLI, and (C) ECG-triggered cMRF and MOLLI; as well as $T_2$ values between (D) cine-MRF and ECG-triggered cMRF, (E) cine-MRF and $T_2$-prepared FLASH, and (F) ECG-triggered cMRF and $T_2$-prepared FLASH. The solid red lines depict the mean bias between any two methods. The dotted red lines show the 95% limits of agreement
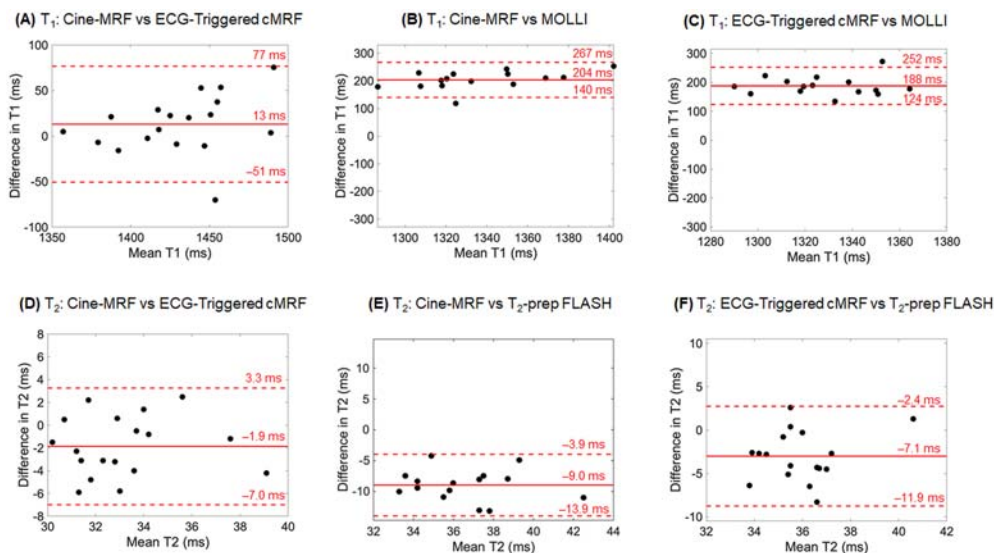


**FIGURE 11** Bland–Altman plots comparing mean systolic myocardial $T_1/T_2$ values. These plots compare $T_1$ values between (A) cine-MRF and ECG-triggered cMRF, (B) cine-MRF and MOLLI, and (C) ECG-triggered cMRF and MOLLI; as well as $T_2$ values between (D) cine-MRF and ECG-triggered cMRF, (E) cine-MRF and $T_2$-prepared FLASH, and (F) ECG-triggered cMRF and $T_2$-prepared FLASH. The solid red lines depict the mean bias between any two methods. The dotted red lines show the 95% limits of agreement

quantifying LV volumes and EF during a 10.9-second breath-hold per slice. This method achieves maps at 1.6 x 1.6 mm$^2$ spatial resolution and 24 cardiac phases, which corresponds to a temporal resolution of 42 ms per frame for a heart rate of 60 bpm. Cine-MRF maps have a shorter effective acquisition window compared with other conventional cardiac mapping sequences, as well as compared with the original implementation of ECG-triggered cMRF with its 250 ms acquisition window, which could reduce blurring and partial volume effects in the myocardium.

This work uses a low-rank reconstruction to recover subspace images at each cardiac phase. Similar to XD-GRASP, the reconstruction exploits correlations along the cardiac motion dimension using temporal finite differences.[30] The subspace images corresponding to the second singular value have an image contrast with bright blood and dark myocardium, similar to the standard bSSFP cine images. The CNR in the MRF-derived cine images is reduced relative to the standard cine images, as quantified by the blood-to-myocardium signal intensity ratio. Nevertheless, the LV volume and EF measurements derived from cine-MRF are in good agreement with those from the standard cine (Figure 14).

Prior work has explored the use of rigid registration for motion correction in brain MRF applications.[47–49] However, one novel aspect of this work is the use of nonrigid registration to align all the cine-MRF images to the same cardiac phase before pattern matching. This step is needed because there are only a few k-space readouts per phase after motion binning (on average, 86 TRs per phase). By using image registration, the entire signal evolution (ie, all 2060 TRs) can be used for pattern matching to generate maps spatially aligned to the same cardiac phase. In addition, the nonrigid displacement fields may provide insight into wall motion abnormalities or myocardial strain, although this was beyond the scope of this study.

Another implementation of free-running cardiac MRF has also been proposed that uses a radial bSSFP MRF acquisition with a 29.4-second breath-hold duration. Maps over eight cardiac phases are obtained using a low-rank tensor reconstruction.[50] One key difference is that the

**FIGURE 12** Intrasubject and intersubject variation for the in vivo study. Intrasubject variation, as quantified by the coefficient of variation (CV), is shown for each method in diastole and systole for (A) T1 and (B) T2. Intersubject variation, as measured by the CV, is shown for each method in diastole and systole for (C) T1 and (D) T2
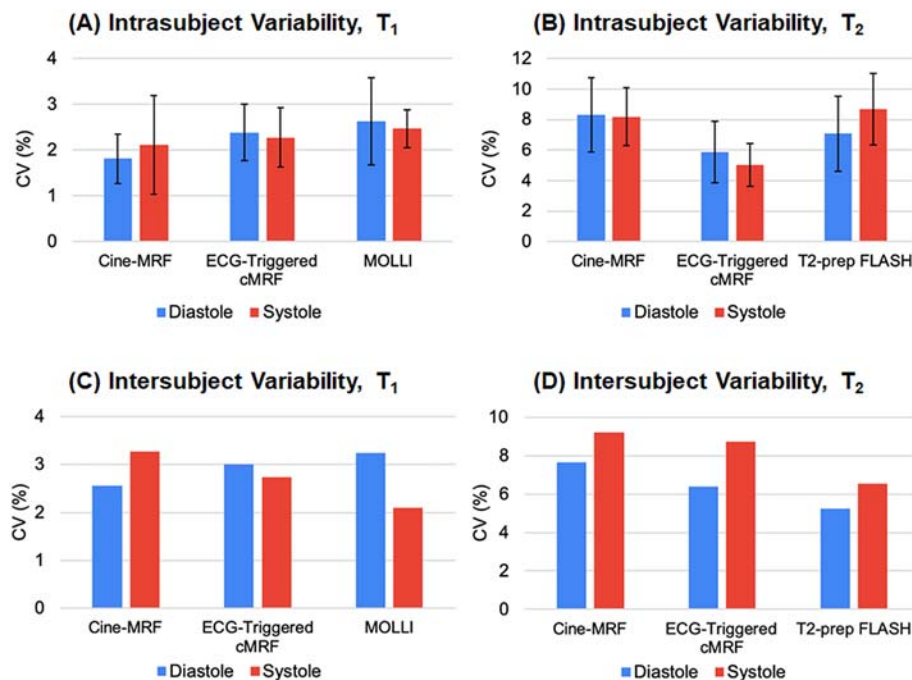


**FIGURE 13** Cine images using cine-MRF and a standard balanced SSFP acquisition. Cine frames during diastole and systole are shown for apical, medial and basal slice positions acquired with (A) cine-MRF and (B) a standard bSSFP cine scan. The measured LV ejection fraction was 55.5% for cine-MRF and 54.0% for the standard cine
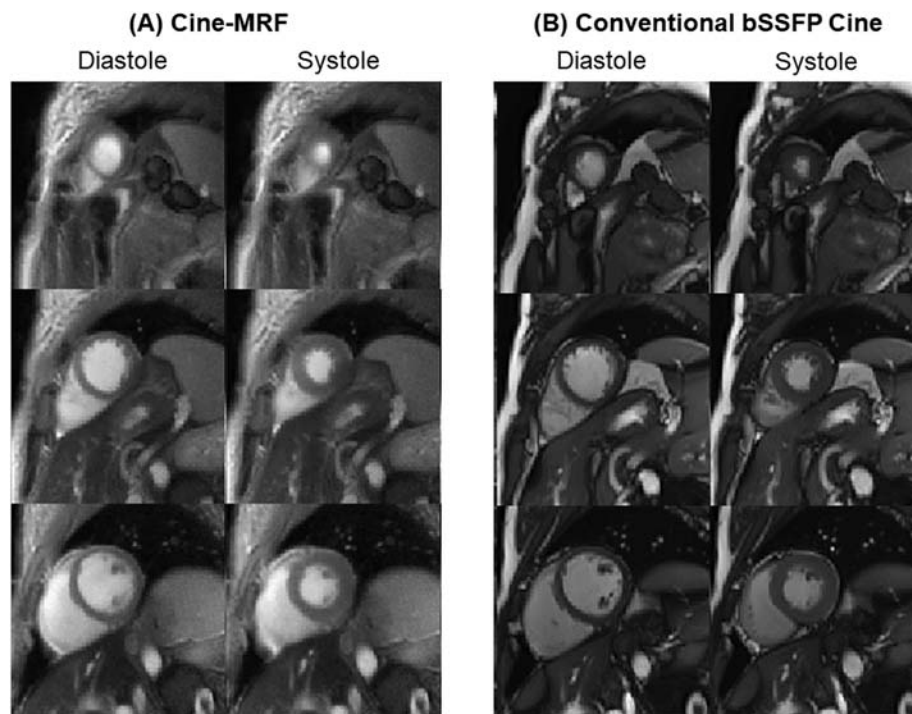


current study uses nonrigid image registration in order to use the entire MRF signal evolution for pattern matching. This enables a higher temporal resolution of 24 phases per cardiac cycle and a shorter breath-hold duration of 10.9 seconds.

Dictionary-based methods like MRF have the potential for reproducible $T_1$ and $T_2$ mapping because sources of measurement error can be modeled in the dictionary. The measurements obtained in this study are consistent with previously published values. This study obtained diastolic/systolic $T_1$ values of 1398/1391 ms with cine-MRF, 1394/1378 ms with ECG-triggered cMRF and 1234/1212 ms with MOLLI; and $T_2$ values of 30.7/30.3 ms with cine-MRF, 32.6/32.9 ms with ECG-triggered cMRF and 37.6/41.0 ms with $T_2$-prepared FLASH. Previous studies at 3 T obtained average $T_1$ values of 1323-1340 ms with ECG-triggered cMRF and 1227-1242 ms with MOLLI, and average $T_2$ values of 34-38 ms with ECG-triggered cMRF and 38 ms with $T_2$-prepared FLASH.[17,32]

As shown in Figures 9-11, the $T_1$ values obtained using cine-MRF are higher than MOLLI, which has been reported previously for ECG-triggered cMRF.[32] One explanation for this difference is that slice profile imperfections and inversion pulse efficiency are modeled in the Bloch
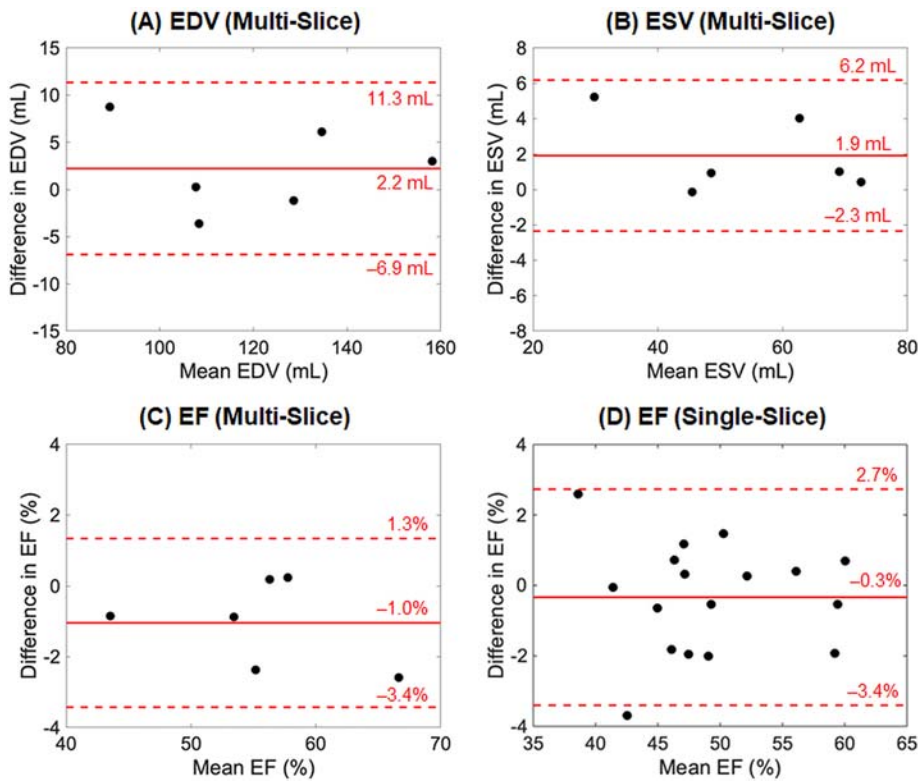
**FIGURE 14** Bland–Altman plots comparing measures of LV function between cine-MRF and a standard bSSFP cine scan. Results are shown for (A) end-diastolic volume, (B) end-systolic volume and (C) ejection fraction over the entire left ventricle for data collected from six healthy subjects. (D) Additionally, results are shown for single-slice ejection fraction measured at a medial slice position for data collected in 17 healthy subjects. The solid red lines indicate the mean bias, and the dotted red lines indicate the 95% limits of agreement

equation simulations when creating the MRF dictionaries, whereas MOLLI does not correct for these factors. These corrections improve accuracy and cause myocardial $T_1$ to increase relative to uncorrected values.[17] The cine-MRF $T_1$ times are lower than values reported using SASHA (1477-1569 ms at 3 T), potentially because cine-MRF uses multiple inversion pulses and may be affected by magnetization transfer.[51,52]

Cine-MRF myocardial $T_2$ times tended to be lower than ECG-triggered cMRF, but this difference was not statistically significant. Both MRF scans did have significantly lower $T_2$ values than $T_2$-prepared FLASH, which has been observed before.[32] The causes for this difference are unclear. Studies in the brain have reported lower $T_2$ values using FISP-MRF compared with standard techniques.[18,53] Some explanations may include motion sensitivity along the unbalanced gradient direction (ie, the slice axis),[26] diffusion weighting from the spoiler gradient,[54] intravoxel dephasing,[55] or magnetization transfer.[56]

One potential source of error not investigated in this study is through-plane motion. Through-plane motion has been shown to cause $T_2$ underestimation when using FISP-MRF in the brain, so it is likely that any through-plane motion during the cine-MRF scan may decrease the apparent $T_2$.[48] Movement of the myocardium in and out of the imaging slice will cause spins to experience an excitation history that is not reflected in the signal model and ultimately lead to inaccurate $T_1$ or $T_2$ measurements. This problem is not unique to cine-MRF and affects other free-running 2D tissue property mapping techniques. This study aims to minimize through-plane errors by using small flip angles for the excitation pulses (less than 15°) and nonselective inversion and $T_2$ preparation pulses. Data are collected during a breath-hold to avoid through-plane motion from respiration. Finally, a relatively large slice thickness (8 mm) is used. Other slice orientations besides short-axis, such as long-axis, sagittal, or coronal, may reduce the amount of through-plane motion caused by cardiac contraction. In the future, extending cine-MRF to a 3D free-breathing technique may circumvent issues related to through-plane motion and improve reproducibility.

Although cine-MRF yields $T_1$ and $T_2$ maps that depict the heart in diastolic or systolic phases, the simulation results in Figure 6 indicate that the relaxation times represent an average over the entire scan. This likely occurs because subspace images from all phases are registered to one target phase before pattern matching, which causes the estimated $T_1$ and $T_2$ values to reflect an average over the cardiac cycle. One potential solution to achieve true cardiac phase-resolved mapping while still maintaining high SNR is to combine motion correction with soft-weighted pattern matching. For example, when generating maps in the diastolic phase, less weight could be given to data acquired in systole, and vice versa.

There are several possibilities for future work. First, the pulse sequence used here was adapted from ECG-triggered cMRF and was not optimized for this application. Numerical optimization of the flip angles, TRs, or preparation pulses could reduce scan time, improve temporal resolution, or increase the sensitivity to $T_1$ and $T_2$. In particular, it may be inefficient to use $T_2$ preparation pulses in cine-MRF because they introduce pauses in data acquisition. Second, cardiac self-gating could be investigated to remove the need for an external ECG, either using the center of k-space,[22,57] image-based navigators,[58] or deep learning.[25] Third, the reconstruction time for cine-MRF is ~ 6 hours per dataset (330 minutes for the low-rank reconstruction, 24 minutes for nonrigid registration, and 3 minutes for pattern matching). Parallel computing and GPU acceleration could make the reconstruction time feasible for clinical use. Fourth, the in vivo results are limited to native $T_1$ and $T_2$ mapping, and future work

will evaluate the accuracy of cine-MRF after injection of gadolinium contrast. Fifth, precision was quantified using the CV, which can also decrease due to overregularization in the low-rank reconstruction. It may be interesting to characterize cine-MRF using alternative measures of precision.[59] Sixth, cine-MRF will be applied in patient studies. This technique may be useful for patients with hypertrophic cardiomyopathy, where there is clinical value in measuring both EF and $T_1$ (and potentially $T_2$).[60] Another application may be imaging after exercise or pharmacological stress, where there is limited time to acquire data while subjects recover towards baseline. Finally, future work will study the feasibility of extending cine-MRF to a free-breathing acquisition for providing simultaneous cine, $T_1$, and $T_2$ maps covering the entire LV using 3D k-space sampling or simultaneous multi-slice (SMS) imaging.[32,61]

## 5 | CONCLUSIONS

In conclusion, a novel extension of MRF, termed cine-MRF, is introduced for simultaneous $T_1$ and $T_2$ mapping and EF quantification. Cine-MRF employs nonrigid registration to align all the imaging data to the same cardiac phase before pattern matching, which improves the image quality and SNR of the $T_1$ and $T_2$ maps. Cine-MRF can potentially streamline the typical cardiac MRI exam workflow by combining functional assessment and relaxation time mapping into one time-efficient acquisition.

### ORCID

*Jesse I. Hamilton* https://orcid.org/0000-0002-4463-481X
*Brendan Eck* https://orcid.org/0000-0003-0971-4432
*Nicole Seiberlich* https://orcid.org/0000-0002-8356-5407

## REFERENCES

1. Bogaert J, Dymarkowski S, Taylor AM, Muthurangu V. *Clinical Cardiac MRI*. 2nd ed. Berlin, Heidelberg: Springer-Verlag; 2012.
2. Hinojar R, Nagel E, Puntmann VO. T1 mapping in myocarditis - headway to a new era for cardiovascular magnetic resonance. *Expert Rev Cardiovasc Ther*. 2015;13(8):871-874.
3. Bull S, White SK, Piechnik SK, et al. Human non-contrast T1 values and correlation with histology in diffuse fibrosis. *Heart*. 2013;99(13):932-937.
4. Goldfarb JW, Arnold S, Han J. Recent myocardial infarction: assessment with unenhanced T1-weighted MR imaging. *Radiology*. 2007;245(1):245-250.
5. Okur A, Kantarcı M, Kızrak Y, et al. Quantitative evaluation of ischemic myocardial scar tissue by unenhanced T1 mapping using 3.0 Tesla MR scanner. *Diagn Interv Radiol*. 20(5):407-413.
6. Karamitsos TD, Piechnik SK, Banypersad SM, et al. Noncontrast T1 mapping for the diagnosis of cardiac amyloidosis. *JACC Cardiovasc Imaging*. 2013;6(4):488-497.
7. Sado DM, White SK, Piechnik SK, et al. Identification and assessment of anderson-fabry disease by cardiovascular magnetic resonance noncontrast myocardial T1 mapping. *Circ Cardiovasc Imaging*. 2013;6(3):392-398.
8. Giri S, Chung Y-C, Merchant A, et al. T2 quantification for improved detection of myocardial edema. *J Cardiovasc Magn Reson*. 2009;11(1):56.
9. Park CH, Choi E-Y, Kwon HM, et al. Quantitative T2 mapping for detecting myocardial edema after reperfusion of myocardial infarction: validation and comparison with T2-weighted images. *Int J Cardiovasc Imaging*. 2013;29(Suppl 1):65-72.
10. Anderson LJ, Holden S, Davis B, et al. Cardiovascular T2-star (T2*) magnetic resonance for the early diagnosis of myocardial iron overload. *Eur Heart J*. 2001;22(23):2171-2179.
11. Butler CR, Savu A, Bakal JA, et al. Correlation of cardiovascular magnetic resonance imaging findings and endomyocardial biopsy results in patients undergoing screening for heart transplant rejection. *J Heart Lung Transplant*. 2015;34(5):643-650.
12. Weingärtner S, Moeller S, Schmitter S, et al. Simultaneous multislice imaging for native myocardial $T_1$ mapping: Improved spatial coverage in a single breath-hold. *Magn Reson Med*. 2017;78(2):462-471.
13. Ma D, Gulani V, Seiberlich N, et al. Magnetic resonance fingerprinting. *Nature*. 2013;495(7440):187-192.
14. Chen Y, Jiang Y, Pahwa S, et al. MR Fingerprinting for Rapid Quantitative Abdominal Imaging. *Radiology*. 2016;279(1):278-286.
15. Rieger B, Akçakaya M, Pariente JC, et al. Time efficient whole-brain coverage with MR Fingerprinting using slice-interleaved echo-planar-imaging. *Sci Rep*. 2018;8(1):1-12.
16. Hamilton JI, Jiang Y, Chen Y, et al. MR fingerprinting for rapid quantification of myocardial T1, T2, and proton spin density. *Magn Reson Med*. 2017;77(4):1446-1458.
17. Hamilton JI, Jiang Y, Ma D, et al. Investigating and reducing the effects of confounding factors for robust T1 and T2 mapping with cardiac MR fingerprinting. *Magn Reson Imaging*. 2018;53:40-51.
18. Ma D, Coppo S, Chen Y, et al. Slice profile and $B_1$ corrections in 2D magnetic resonance fingerprinting. *Magn Reson Med*. 2017;78(5):1781-1789.
19. Buonincontri G, Schulte RF, Cosottini M, Tosetti M. Spiral MR fingerprinting at 7 T with simultaneous B1 estimation. *Magn Reson Imaging*. 2017;41:1-6.

20. Weingärtner S, Shenoy C, Rieger B, Schad LR, Schulz-Menger J, Akçakaya M. Temporally resolved parametric assessment of Z-magnetization recovery (TOPAZ): Dynamic myocardial T 1 mapping using a cine steady-state look-locker approach. *Magn Reson Med*. 2018;79(4):2087-2100.

21. Becker KM, Schulz-Menger J, Schaeffter T, Kolbitsch C. Simultaneous high-resolution cardiac T1 mapping and cine imaging using model-based iterative image reconstruction. *Magn Reson Med*. 2019;81(2):1080-1091.

22. Qi H, Jaubert O, Bustin A, et al. Free-running 3D whole heart myocardial T1 mapping with isotropic spatial resolution. *Magn Reson Med*. 2019;82(4): 1331-1342.

23. Qi H, Bustin A, Cruz G, et al. Free-running simultaneous myocardial T1/T2 mapping and cine imaging with 3D whole-heart coverage and isotropic spatial resolution. *Magn Reson Imaging*. 2019;63:159-169.

24. Christodoulou AG, Shaw JL, Nguyen C, et al. Magnetic resonance multitasking for motion-resolved quantitative cardiovascular imaging. *Nat Biomed Eng*. 2018;2(4):215-226.

25. Shaw JL, Yang Q, Zhou Z, et al. Free-breathing, non-ECG, continuous myocardial T1 mapping with cardiovascular magnetic resonance multitasking. *Magn Reson Med*. 2019;81(4):2450-2463.

26. Jiang Y, Ma D, Seiberlich N, Gulani V, Griswold MA. MR fingerprinting using fast imaging with steady state precession (FISP) with spiral readout. *Magn Reson Med*. 2015;74(6):1621-1631.

27. Brittain JH, Hu BS, Wright GA, Meyer CH, Macovski A, Nishimura DG. Coronary angiography with magnetization-prepared T2 contrast. *Magn Reson Med*. 1995;33(5):689-696.

28. Hargreaves B. Variable-Density Spiral Design Functions. http://mrsrl.stanford.edu/~brian/vdspiral/. 2005. Accessed June 1, 2017.

29. Winkelmann S, Schaeffter T, Koehler T, Eggers H, Doessel O. An optimal radial profile order based on the Golden Ratio for time-resolved MRI. *IEEE Trans Med Imaging*. 2007;26(1):68-76.

30. Feng L, Axel L, Chandarana H, Block KT, Sodickson DK, Otazo R. XD-GRASP: Golden-angle radial MRI with reconstruction of extra motion-state dimensions using compressed sensing. *Magn Reson Med*. 2016;75(2):775-788.

31. Assländer J, Cloos MA, Knoll F, Sodickson DK, Hennig J, Lattanzi R. Low rank alternating direction method of multipliers reconstruction for MR fingerprinting. *Magn Reson Med*. 2018;79(1):83-96.

32. Hamilton JI, Jiang Y, Ma D, et al. Simultaneous multislice cardiac magnetic resonance fingerprinting using low rank reconstruction. *NMR Biomed*. 2019; 32(2):e4041.

33. Doneva M, Amthor T, Koken P, Sommer K, Börnert P. Matrix completion-based reconstruction for undersampled magnetic resonance fingerprinting data. *Magn Reson Imaging*. 2017;41:41-52.

34. Zhao B, Bilgic B, Adalsteinsson E, Griswold MA, Wald LL, Setsompop K. Simultaneous multislice magnetic resonance fingerprinting with low-rank and subspace modeling. In: *2017 39th Annual International Conference of the IEEE Engineering in Medicine and Biology Society (EMBC)*. Vol 2017. IEEE; 2017: 3264-3268.

35. McGivney DF, Pierre E, Ma D, et al. SVD compression for magnetic resonance fingerprinting in the time domain. *IEEE Trans Med Imaging*. 2014;33 (12):2311-2322.

36. Fessler J, Sutton B. Nonuniform fast Fourier transforms using min-max interpolation. *IEEE Trans Signal Process*. 2003;51(2):560-574.

37. Walsh D, Gmitro A, Marcellin M. Adaptive reconstruction of phased array MR imagery. *Magn Reson Med*. 2000;43(5):682-690.

38. Lustig M, Donoho D, Pauly JM. Sparse MRI: The application of compressed sensing for rapid MR imaging. *Magn Reson Med*. 2007;58(6):1182-1195.

39. Modat M, Ridgway GR, Taylor ZA, et al. Fast free-form deformation using graphics processing units. *Comput Methods Programs Biomed*. 2010;98(3): 278-284.

40. Clayden J. CRAN- Package RNiftyReg. https://cran.r-project.org/package=RNiftyReg. 2019. Accessed June 24, 2019.

41. Wissmann L, Santelli C, Segars WP, Kozerke S. MRXCAT: Realistic numerical phantoms for cardiovascular magnetic resonance. *J Cardiovasc Magn Reson*. 2014;16(1):63.

42. Russek SE, Boss M, Jackson EF, et al. Characterization of NIST/ISMRM MRI System Phantom. In: *Proc. 20th Annu. Meet. ISMRM*. Melbourne, Australia; 2012:2456.

43. Bland JM, Altman DG. Statistical methods for assessing agreement between two methods of clinical measurement. *Lancet*. 1986;1(8476):307-310.

44. Siemens Medical Solutions USA. MyoMaps. https://usa.healthcare.siemens.com/magnetic-resonance-imaging/options-and-upgrades/clinical-applications/myomaps. 2018. Accessed February 27, 2018.

45. Messroghli DR, Radjenovic A, Kozerke S, Higgins DM, Sivananthan MU, Ridgway JP. Modified Look-Locker inversion recovery (MOLLI) for high-resolution T1 mapping of the heart. *Magn Reson Med*. 2004;52(1):141-146.

46. Cerqueira MD. Standardized Myocardial Segmentation and Nomenclature for Tomographic Imaging of the Heart: A Statement for Healthcare Professionals From the Cardiac Imaging Committee of the Council on Clinical Cardiology of the American Heart Association. *Circulation*. 2002;105(4): 539-542.

47. Mehta BB, Ma D, Pierre EY, Jiang Y, Coppo S, Griswold MA. Image reconstruction algorithm for motion insensitive MR Fingerprinting (MRF): MORF. *Magn Reson Med*. 2018;80(6):2485-2500.

48. Cruz G, Jaubert O, Schneider T, Botnar RM, Prieto C. Rigid motion-corrected magnetic resonance fingerprinting. *Magn Reson Med*. 2018;81(2): 947-961.

49. Xu Z, Ye H, Lyu M, et al. Rigid motion correction for magnetic resonance fingerprinting with sliding-window reconstruction and image registration. *Magn Reson Imaging*. 2019;57:303-312.

50. Jaubert O, Cruz G, Bustin A, et al. Free-running cardiac magnetic resonance fingerprinting: Joint T1/T2 map and Cine imaging. *Magn Reson Imaging*. 2020;68:173-182.

51. Weingärtner S, Meßner NM, Budjan J, et al. Myocardial T1-mapping at 3T using saturation-recovery: reference values, precision and comparison with MOLLI. *J Cardiovasc Magn Reson*. 2016;18(1):84.

52. Robson MD, Piechnik SK, Tunnicliffe EM, Neubauer S. T1 measurements in the human myocardium: The effects of magnetization transfer on the SASHA and MOLLI sequences. *Magn Reson Med*. 2013;70(3):664-670.

53. Ma D, Jiang Y, Chen Y, et al. Fast 3D magnetic resonance fingerprinting for a whole-brain coverage. *Magn Reson Med*. 2018;79(4):2190-2197.

54. Kobayashi Y, Terada Y. Diffusion-weighting caused by spoiler gradients in the fast imaging with steady-state precession sequence may lead to inaccurate T2 measurements in MR fingerprinting. *Magn Reson Med Sci*. 2019;18(1):96-104.

55. Assländer J, Glaser SJ, Hennig J. Pseudo steady-state free precession for MR-fingerprinting. *Magn Reson Med*. 2017;77(3):1151-1161.

56. Gloor M, Scheffler K, Bieri O. Quantitative magnetization transfer imaging using balanced SSFP. *Magn Reson Med*. 2008;60(3):691-700.

57. Zhou R, Yang Y, Mathew RC, et al. Free-breathing cine imaging with motion-corrected reconstruction at 3T using SPiral Acquisition with Respiratory correction and Cardiac Self-gating (SPARCS). *Magn Reson Med*. 2019;82(2):706-720.

58. Larson AC, White RD, Laub G, McVeigh ER, Li D, Simonetti OP. Self-gated cardiac cine MRI. *Magn Reson Med*. 2004;51(1):93-102.

59. Roujol S, Weingärtner S, Foppa M, et al. Accuracy, precision, and reproducibility of four T1 mapping sequences: a head-to-head comparison of MOLLI, ShMOLLI, SASHA, and SAPPHIRE. *Radiology*. 2014;272(3):683-689.

60. Dass S, Suttie JJ, Piechnik SK, et al. Myocardial tissue characterization using magnetic resonance noncontrast T1 mapping in hypertrophic and dilated cardiomyopathy. *Circ Cardiovasc Imaging*. 2012;5(6):726-733.

61. Barth M, Breuer F, Koopmans PJ, Norris DG, Poser BA. Simultaneous multislice (SMS) imaging techniques. *Magn Reson Med*. 2015;75(1):63-81.

## SUPPORTING INFORMATION

Additional supporting information may be found online in the Supporting Information section at the end of this article.